



RESEARCH ARTICLE

Plasma-based tunable relativistic laser focusing and strong axial magnetic field generation

Lingyu Zhang^{®†}, Hao Zhang^{®†}, Jingyi Wang, Xinyan Li[®], and Tong-Pu Yu[®]

Department of Physics, National University of Defense Technology, Changsha, China (Received 7 May 2025; revised 17 June 2025; accepted 22 July 2025)

Abstract

Precise control of the laser focal position in the relativistic laser–plasma interaction is crucial for electron acceleration, inertial confinement fusion, high-order harmonic generation, etc. However, conventional methods are characterized by limited tunability and rapid divergence of the relativistic laser pulse after passing through a single focal point. In this work, we propose a novel plasma lens with a density gradient to achieve laser focusing in a tunable focal volume. The capacity depends on the modification of the phase velocity of the incident seed laser propagating in plasma. By modifying the plasma density gradient, one can even achieve an off-axis focusing plasma lens, allowing the laser to be focused further at an adjustable focus. Based on this new type of optical device, a beam-splitting array is also proposed to leverage this unique focusing mechanism for the generation of strong axial magnetic fields (>1000 T). Three-dimensional particle-in-cell simulations demonstrate that the seed laser with a focal spot of 9 μ m passing through the density varying plasma lens exhibits a focused laser with a focal spot of approximately 2.3 μ m and an 18 times enhancement of the laser intensity. The approach has considerable potential for applications in several areas, including laser-driven particle acceleration, X/γ -ray emission, strong magnetic field generation, etc.

Keywords: axial magnetic field; laser-plasma interaction; off-axis focusing; plasma lens; tunable focal volume

1. Introduction

In recent decades, there has been a notable advancement in the field of laser technology, with the emergence of revolutionary new techniques and applications, for example, chirped pulse amplification (CPA)^[1] and optical parametric chirped pulse amplification (OPCPA)^[2], paving the way for novel avenues of fundamental research in domains such as high-energy-density physics^[3–7], laser-assisted nuclear physics^[8–10] and attosecond science^[11]. The Station of Extreme Light (SEL) has been upgraded to allow for the amplification of laser focusing intensity up to 10²⁴ W/cm², with a power output of up to 100 PW^[12]. However, due to the damage thresholds of conventional solid-state optical components, the generation and manipulation of highintensity laser pulses have become progressively more arduous as the peak intensity of lasers increases. To address this challenge, extensive research has been conducted on plasma-based optical components, a new concept of novel optical devices, which offer damage thresholds several orders of magnitude higher than those of solid-state optics^[13–17]. Over the past two decades, various advanced plasma-based optical elements have been shown to effectively regulate the temporal contrast^[13], phase^[14], polarization^[15], duration^[16] and intensity^[17] of relativistic laser pulses. In particular, the utilization of plasma to focus laser pulses as a means of modulation to augment laser intensity has recently garnered considerable attention^[18–28].

Due to the small focal spots and exceptionally high intensity, focused lasers have a wide range of applications in fields as diverse as novel particle accelerators [29–32], high-order harmonics [33–35], X/γ -ray generation [36–38] and inertial confinement fusion [39,40]. The focusing of a laser pulse can normally be categorized into two distinct types: axial focusing and off-axis focusing. Axial focusing involves the concentration of the laser beam along the propagation axis, whereas off-axis focusing results in a laser beam focusing away from the propagation axis. Up to now, a plethora of studies have already been conducted to focus relativistic laser pulses axially [18–28,41], for example, plasma mirrors [18], plasma tapered-channels [19], plasma gratings [20], plasma lenses [21–23], relativistic plasma apertures [24], plasma zone plates [25,26] and plasma-based multiple-beam focus [27,28].

© The Author(s), 2025. Published by Cambridge University Press in association with Chinese Laser Press. This is an Open Access article, distributed under the terms of the Creative Commons Attribution licence (https://creativecommons.org/licenses/by/4.0), which permits unrestricted re-use, distribution and reproduction, provided the original article is properly cited.

Correspondence to: T. P. Yu and X. Li, Department of Physics, National University of Defense Technology, Changsha 410073, China. Emails: tongpu@nudt.edu.cn (T. P. Yu); ustclxy@mail.ustc.edu.cn (X. Li)

[†]These authors contributed equally to this work.

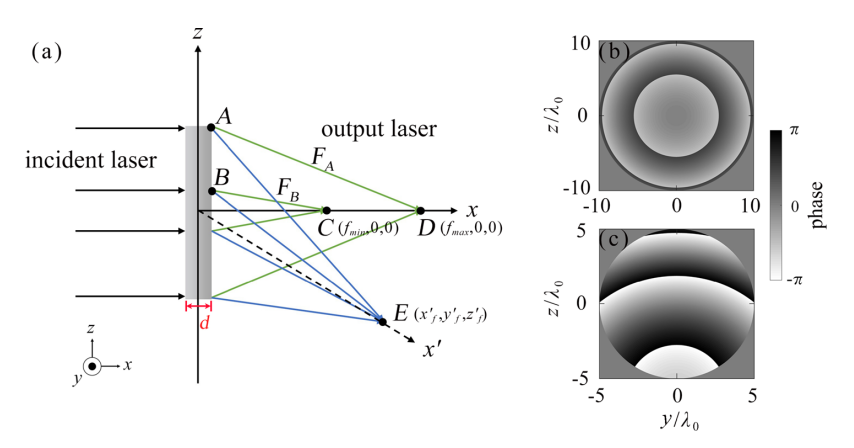


Figure 1. (a) Schematic representation of the ability of the proposed novel plasma lens with a density gradient. The plasma lens can focus the output laser at the designated locations $C(f_{\min}, 0, 0)$, $D(f_{\max}, 0, 0)$ and $E(x_f, 0, 0)$, respectively. (b) Phase profiles of the axial focusing plasma lens and (c) the off-axis focusing plasma lens.

Plasma, as an optical component to focus the laser, has been demonstrated to substantially reduce the focal spot radius and augment the laser intensity. However, in these approaches the laser pulse is focused on a single focal point, and the focus position cannot be arbitrarily adjusted. In comparison with axial focusing, off-axis focusing has been shown to offer a number of advantages. These include a wider field of view, better aberration correction, shorter optical paths and higher resolution^[42–45]. In particular, it is also possible to focus a laser pulse on a specified position^[46–48], promising many potential applications in, for example, spectrometers^[46], wavelength demultiplexers^[47] and head-mounted displays^[48]. Nevertheless, there is currently no effective method for achieving off-axis focusing at relativistic laser intensity using plasma.

Here, we propose a novel plasma lens with a density gradient to achieve laser pulse focusing in a tunable focal volume efficiently. In this scenario, the phase velocity of laser propagation in the plasma is well controlled by adjusting the density distribution of the plasma lens, enabling the laser to focus in a tunable focal volume. This tunable characteristic enables precise control over electron trapping and acceleration, holding great potential for generating highquality, stable and tunable electron beams^[49]. Furthermore, it may allow the optimization of laser ignition efficiency through controlled adjustment of the focal length^[50]. Using such a plasma lens with tunable density distribution, we also achieve off-axis focusing, allowing the laser to be focused further at an adjustable focus, as schematically shown in Figure 1. Three-dimensional particle-in-cell (3D-PIC) simulations demonstrate that an incident Gaussian laser with the intensity of 1.3×10^{18} W/cm² passing through the plasma lens can attain laser focusing within a tunable focal volume, leading to an output intensity of 2.34×10^{19} W/cm² (~18 times enhancement). The energy transmission efficiency to the output laser is up to 61.16%. With such an off-axis focusing lens, we have devised a beam-splitting array that enables the generation of a strong axial magnetic field (>1000 T). This capability may manifest its advantages in future experiments aimed at inertial confinement fusion^[51,52], laser-driven ion acceleration^[53], magnetized atomic physics^[54], etc.

2. Theory and numerical simulation

The incident laser phase velocity v_p is modulated by the density distribution of the proposed novel plasma lens, in accordance with the formula $v_p = c/\sqrt{1 - n_e/\gamma_L n_c}$ ^[55]. Here n_e is the local electron density of plasma, $n_c =$ $(m_e \omega_0^2) / (4\pi e^2) = 1.1 \times 10^{21}$ cm⁻³ is the critical density corresponding to laser wavelength $\lambda_0 = cT_0$, e is the unit charge, c is the speed of light in vacuum, m_e is the electron mass, ω_0 is the laser frequency, T_0 is the laser cycle, $\gamma_L = \sqrt{1 + a^2/2}$ is the relativistic factor for a linearly polarized (LP) laser, $a = a_0 \exp(-(r/\sigma_0)^2)$ is the transverse electric field distribution of the Gaussian laser, $a_0 = (eE_0) / (m_e c\omega_0)$ is the laser electric field normalized amplitude, E_0 is the electric field amplitude, r is the distance with regard to the optical axis and σ_0 is the focal radius of the Gaussian laser. The passage of Gaussian laser pulses through the plasma lens follows Fermat's principle^[56]:

$$\mu_A d + F_A = \mu_B d + F_B. \tag{1}$$

Here, d denotes the thickness of the plasma lens, while μ_A and μ_B represent the refractive indices at two arbitrary positions A and B on the plasma lens. The variables F_A and F_B signify the distances from these two points to the focal point. Figure 1(a) illustrates the laser focusing principle in a schematic way, while Figures 1(b) and 1(c) present the phase distributions of plasma lenses with distinct focusing capacities. Since the refractive index follows $\mu = c/v_p$, this allows for a radial variation in the plasma density. Therefore, to achieve laser focusing at a designated position, we can fix the refractive index distribution of the lens using

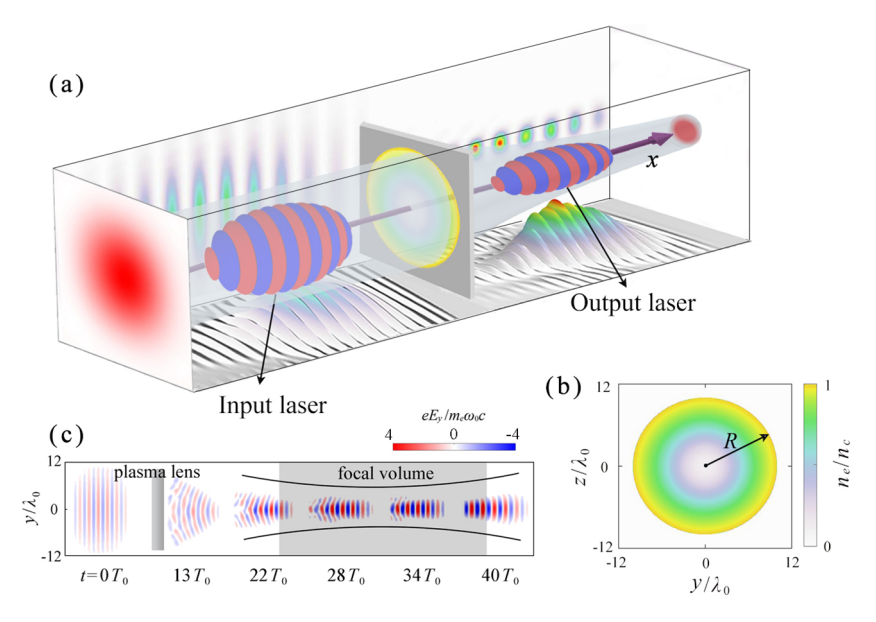


Figure 2. (a) Schematic diagram of an incident laser irradiating a density varying plasma lens to produce a focusing output laser. The projections in front of and behind the box are the electric field distributions on the (y, z) plane of the incident and the output laser, respectively. The 3D electric field distributions of the incident and output laser are shown along the direction of laser propagation. The laser intensity distributions of the incident and output laser are shown at the bottom of the box. (b) Density distribution of the plasma lens as used in (a). (c) Evolution of the laser electric field distributions E_y on the (x, y) plane.

Equation (1), which introduces a spatially varying phase delay, enabling precise laser focusing at the desired position. By establishing the minimum density of the plasma lens (n_0) , it becomes possible to get the plasma density of the lens at any given point by the following:

$$n_{\rm e} = \gamma_{\rm L} n_{\rm c} \left(1 - \left(\sqrt{1 - \frac{n_0}{\gamma_{\rm L} n_{\rm c}}} - \frac{\sqrt{r^2 + f_{\rm m}^2} - f_{\rm m}}{d} \right) \right),$$
 (2)

where $f_{\rm m}$ is the corresponding focal length, ranging from $f_{\rm min}$ to $f_{\rm max}$. Figure 2 illustrates the focal volume of the laser focusing after the laser passes through the plasma lens.

The proposed methodology has been demonstrated using 3D-PIC simulations performed with the relativistic electromagnetic code EPOCH^[57]. In our simulations, the grid size of the simulation box is 40 μ m \times 24 μ m \times 24 μ m in the $x \times y \times z$ directions, which is sampled by $800 \times 480 \times 480$ cells with six macro-particles per cell. The incident laser is an LP Gaussian laser pulse with the wavelength of λ_0 1 μ m and a focal radius of $\sigma_0 = 9\lambda_0$. The laser initiates its propagation along the x-direction from the left-hand boundary at t = 0. The incident laser electric field normalized amplitude is $a_0 = 1$, and full duration is $\tau = 6T_0$. The laser– target interaction is schematically shown in Figure 2(a), with the target composed of fully ionized carbon ions, hydrogen ions and electrons. As illustrated in Figure 2(b), the plasma density distribution exhibits a gradient along the radial direction within a plasma lens radius $R = 10\lambda_0$. The plasma density follows the gradient as defined by Equation (2), with a minimum value of $n_0 = 0.1n_c$ and a maximum value of $0.92n_{\rm c}$. In the simulations, one sees that the plasma lens can focus the laser in a designed focal volume, which can be tuned from $f_{\rm min}$ to $f_{\rm max}$, for example, $f_{\rm min}=20\lambda_0$ and $f_{\rm max}=30\lambda_0$. Figure 2(c) schematically illustrates the evolution of laser focusing. The lens is located between $x=3\lambda_0$ and $x=5.5\lambda_0$ with the thickness of $d=2.5\lambda_0$. In the experiment, the aerofluorescent graphene substrate can be utilized, boasting a density as low as 0.16 kg/m^3 , corresponding to a fully ionized plasma density of $0.028n_{\rm c}^{[58-60]}$. This substrate exhibited commendable conductivity and thermal stability. The 3D printing technique may be employed to prepare the plasma lens with a density gradient as expected in our scenario^[61-63].

Figure 3(a) shows the intensity evolution of the output laser in the (x,y) plane at five different times from $t=8T_0$ to $34T_0$. The incident laser pulse is progressively focused after passing through the plasma lens, resulting in a gradual increase in the laser intensity. At $t=34T_0$, the peak intensity of the output laser can reach 2.34×10^{19} W/cm², an order of magnitude higher than the incident laser pulse. In order to assess the plasma lens performance, the Fresnel–Kirchhoff diffraction formula is used to predict analytically the electric field component of the output laser. Here, the diffracted electric field can be expressed as follows [64]:

$$E(y,z) = \frac{1}{i\lambda_0} \iint u_0(y',z') t(y',z') k(\theta) \frac{\exp(ik\rho)}{\rho} dy' dz', \quad (3)$$

where $\rho = \sqrt{(x-x')^2 + (y-y')^2 + (z-z')^2}$, $u_0(y',z') = a$ represents the transverse electric field distribution of the incident Gaussian laser, $k(\theta) = \frac{\cos(n,r) - \cos(n,r_0)}{2}$ is the inclination factor with (n,r) the angle at which the laser deviates from the original optical path after diffraction occurs in

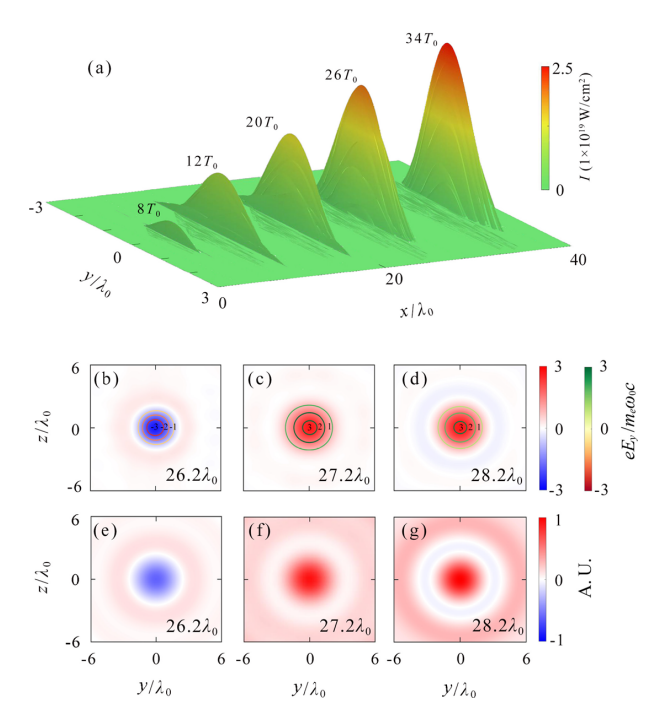


Figure 3. (a) Evolution of the output laser intensity I from $t = 8T_0$ to $34T_0$. (b)–(d) The transverse electric field distribution of E_y at different sections from $x = 26.2\lambda_0$ to $28.2\lambda_0$ at $t = 30T_0$ (simulation results). The transverse circles represent the laser intensity contours. (e)–(g) The same as (b)–(d), but from the Fresnel–Kirchhoff diffraction formula.

the plasma lens and (n, r_0) is the angle at which the laser reaches the plasma lens from the laser source. Here, the phase modulation function t(y', z') of the plasma lens can be obtained by the following^[65]:

$$t(y',z') = \frac{2\pi}{\lambda_0} \left(f_{\rm m} - \sqrt{(x-x')^2 + (y-y')^2 + (z-z')^2} \right). \tag{4}$$

The phase changes of the laser pulse after passing through plasma lenses with varying density distribution are shown in Figures 1(b) and 1(c).

Figures 3(b)-3(d) show the evolution of the transverse electric field distribution in the simulations, while Figures 3(e)-3(g) show the theoretical results from Equation (3). It can be observed that both agree remarkably well with each. This indicates that the laser focusing was realized by the incident laser passing through the proposed plasma lens.

According to Equation (2), the density of the plasma lens is determined by both the incident laser and the target parameters. In practice, the laser pre-pulse may influence the lens design to some extent. Presently, ultra-intense fs lasers have achieved significantly improved contrast ratios, allowing our scheme to design the lens and control the focal position with greater precision. Figure 4(a) shows the effects of the plasma lens thickness d, incident laser focal radius σ_0 and the maximum value of the focal volume f_{max} on the

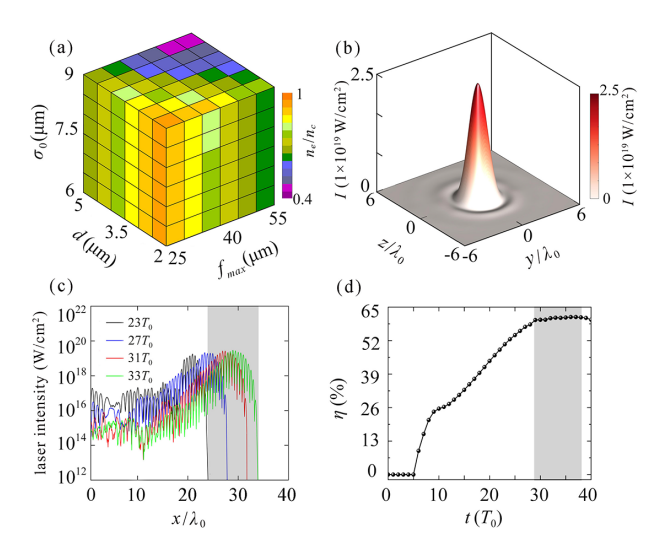


Figure 4. (a) Effects of plasma lens thickness d ($2\lambda_0$ to $5\lambda_0$), laser spot size σ_0 ($6\lambda_0$ to $9\lambda_0$) and the maximum value of the focal volume f_{max} ($25\lambda_0$ to $55\lambda_0$) on the maximum density of the plasma lens when the incident laser parameter is $a_0 = 1$. (b) Transverse section of the output laser intensity at $x = 28\lambda_0$ and $t = 33T_0$. (c) Distribution of the laser intensity along the x-axis from $t = 23T_0$ to $33T_0$. (d) Evolution of the laser energy transmission efficiency from the incident laser pulse to the output laser pulse (here, the gray area marks the distribution of the focal volume along the x-axis).

maximum density of the plasma lens when the incident laser parameter is $a_0 = 1$. The objective of this study is to evaluate the extent to which the three parameters under consideration affect the plasma density of the lens. We investigated the change in the plasma density of the lens on the (d, f_{max}) , (d, σ_0) and $(f_{\text{max}}, \sigma_0)$ planes by selecting six points each in the ranges from $d=2\lambda_0$ to $2.5\lambda_0$, $\sigma_0=6\lambda_0$ to $9\lambda_0$ and $f_{\text{max}} = 25\lambda_0$ to $55\lambda_0$. As illustrated in Figure 4(a), the variation in plasma density is found to be minimally affected by the parameter σ_0 when either d or f_{max} is kept constant, for both (d, σ_0) and $(f_{\text{max}}, \sigma_0)$ planes. This indicates that the plasma density is primarily controlled by the thickness d of the plasma lens and the maximum value of the focal volume f_{max} , insensitive to the incident laser focal radius σ_0 . Figures 4(b) and 4(c) show the intensity distribution of the output laser in the transverse section at $x = 28\lambda_0$ ($t = 33T_0$) and along the x-axis, respectively. The results indicate that when $x = 23\lambda_0$, the intensity of the output laser is significantly enhanced within the focal volume region. This demonstrates a long focal volume of the output laser pulse produced, which is a unique feature of the plasma lens proposed. Due to the focusing capability of the plasma lens, the intensity of the resulting focused laser can reach 10^{19} W/cm², with a focal radius of approximately $2.3\lambda_0$. In addition, the evolution of the laser energy transmission efficiency was also investigated. Here, the total electromagnetic energy of the output laser can be calculated as $E_{\text{laser}} = \frac{1}{2} \int \left(\varepsilon_0 \mathbf{E}^2 + (1/\mu_0) \mathbf{B}^2 \right) dV$, with ε_0 the permittivity of vacuum and μ_0 the permeability of vacuum. As shown in Figure 4(d), the output laser maintains a high-energy

Table 1. The maximum density $(n_{e, \max})$ of the plasma lens corresponding to different laser electric field normalized amplitudes (a_0) and thicknesses of the plasma lens (d).

a_0	$d(\lambda_0)$	$n_{\rm e,max}(n_{\rm c})$
1	2	0.99
1	2.5	0.92
1	3	0.84
1	4	0.70
1	5	0.61
3	2.5	1.04
5	2.5	1.34
7	2.5	1.74
10	2.5	2.38

transmission efficiency within the focal volume, reaching a maximum of 61.16% at $t = 36T_0$. There has been a lot of previous work using plasma lenses to achieve laser pulse amplification; for instance, some have demonstrated that the energy transmission efficiency of laser focusing using a holographic plasma lens is approximately 65%^[41], while employing a laser-driven plasma lens can enhance the efficiency to nearly 60%^[21]. Obviously, the energy transmission efficiency achieved via our proposed scheme is comparable to the existing research results. However, except for the laser focusing capability, our proposed scheme offers a distinct advantage: it enables laser focusing within a tunable focal volume and maintains a high laser intensity distribution throughout the focal volume. This effectively avoids the issue of rapid divergence of the laser pulse after passing through the focal point and achieves control of the focus position, expanding its application potential in particle acceleration^[66,67], inertial confinement fusion^[68], etc.

The effects of the incident laser parameter a_0 and the thickness of the plasma lens d on the focused laser were also investigated. According to Equation (2), the density of the plasma lens varies with changes in the incident laser relativistic factor γ_L and the plasma lens thickness d. Furthermore, γ_L is governed by the a_0 . Table 1 presents the maximum density of the plasma lens corresponding to different a_0 and d values. The effect of the incident laser parameter a_0 on the energy transmission efficiency η (black circles), the ratio of the focused laser intensity to the incident laser intensity I/I_0 (red circles) and the focal radius σ_0 (blue circles) of the focused laser, as shown in Figure 5(a), are discussed. It can be seen that when the incident laser parameter $a_0 = 1$, the energy transmission efficiency reaches 61.16% and the focal radius can be reduced to approximately $2.3\lambda_0$. The corresponding ratio of the intensity of the focused laser to the incident Gaussian laser is as high as 18. As the intensity of the incident laser increases, the laser is still amplified. The simulation results demonstrate that the plasma lens designed can still achieve a focusing function at the incident laser parameter of $a_0 = 10$. However, as

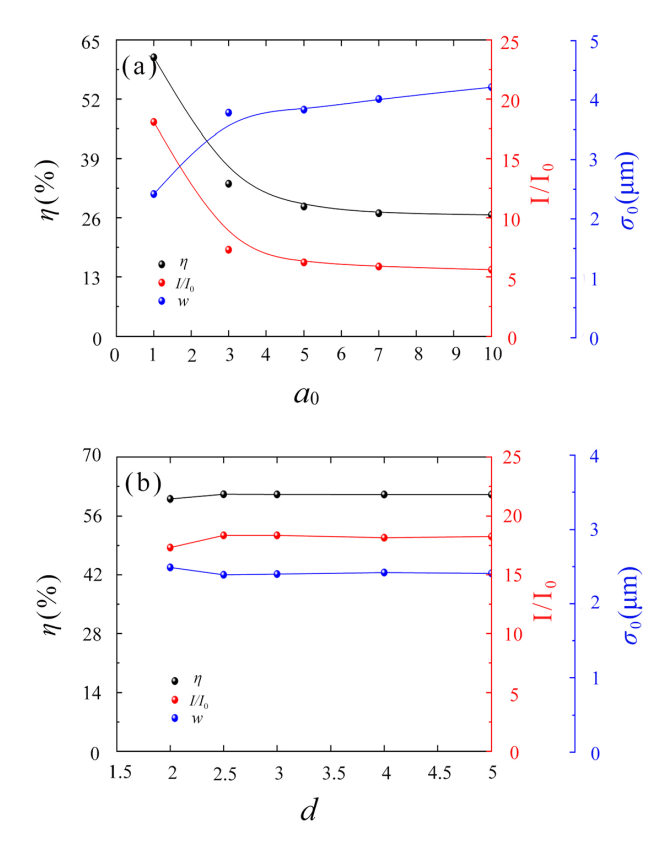


Figure 5. The laser energy transmission efficiency to the output laser $(\eta, \text{black circles})$, the ratio of the output laser intensity to the incident laser intensity $(I/I_0, \text{red circles})$ and the output laser focal radius $(\sigma_0, \text{blue circles})$ varying with (a) the laser electric field normalized amplitude a_0 and (b) the thickness of the plasma lens $d(a_0 = 1)$.

the incident laser intensity rises, controlling the laser focal volume becomes challenging. Through additional 3D-PIC simulations, it is found that the plasma lens can maintain the focused laser intensity within a desired focal volume when $a_0 \leq 20$. Figure 5(b) demonstrates the impact of the thickness d on the energy transmission efficiency, the amplification factor and the focal radius of the focused laser. One sees that at $a_0 = 1$, variations in thickness result in only minor alterations to the energy transmission efficiency, magnification ratio and focal radius of the focused laser. This validates the robustness of the plasma lens proposed in our scenario.

3. Off-axis relativistic laser focusing via the density gradient plasma lens

By leveraging the controllable focal position characteristics, our scheme can also achieve off-axis focusing. The density of the plasma lens designed in our study is adjustable, allowing for the control of the phase velocity of laser propagation in the plasma by changing the density gradient of the plasma lens. This process alters the refractive index of the plasma lens and focuses the laser to an adjustable off-axis

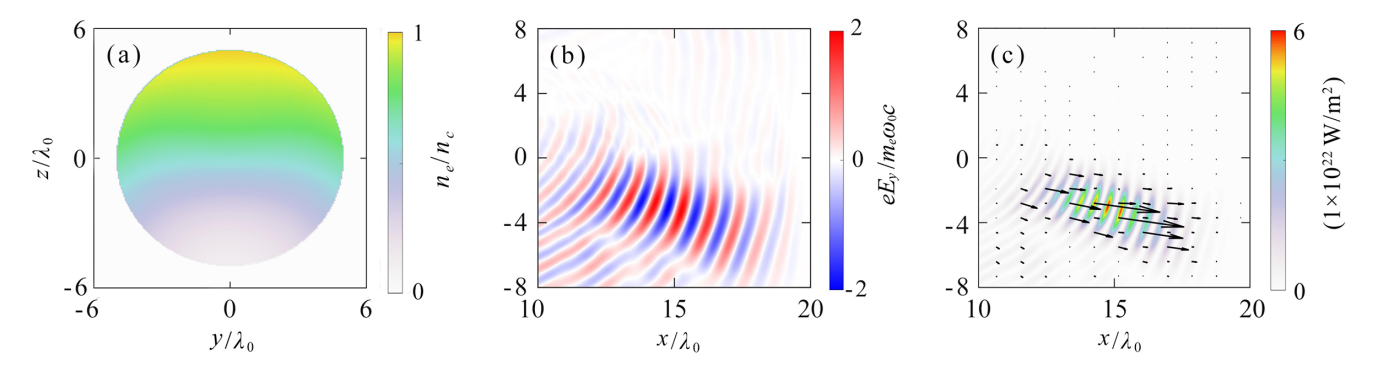


Figure 6. (a) Plasma density distribution of the off-axis focusing plasma lens. (b) Electric field distribution E_y of the output laser on the (x, z) plane between $x = 10\lambda_0$ and $20\lambda_0$ at $t = 20T_0$. (c) Poynting vector S on the (x, z) plane between $x = 10\lambda_0$ and $20\lambda_0$ at $t = 20T_0$. Here, the arrows represent the direction of the Poynting vector.

position $E(x'_f, y'_f, z'_f)$, as schematically shown in Figure 1. In our simulations, the focus position is $(21\lambda_0, 0\lambda_0, -6\lambda_0)$. Figure 6(a) illustrates the density distribution of the offaxis focusing plasma lens. Here, the radius of the plasma lens is set with $R = 5\lambda_0$, the thickness $d = 3\lambda_0$, the density distribution follows Equation (2) and the minimum density $n_0 = 0.1 n_c$. Figures 6(b) and 6(c) depict the distributions of the electric field and the Poynting vector of the output laser in the (x, z) plane, respectively. Here, the Poynting vector can be calculated by $S = E \times B$, with E and B being the electric and magnetic fields, respectively. The distributions are shown at the moment after the incident laser has passed through the plasma lens at $t = 20T_0$. It can be observed from Figure 6(b) that the propagation direction of the laser is significantly deflected toward the focal position after traversing the plasma lens. The arrows in Figure 6(c) represent the direction of the Poynting vector, directed toward the focus, providing further evidence of the efficacy of the off-axis focusing ability. To the best of our knowledge, this is the first proposed use of the plasma lens for off-axis focusing, which may have potential applications in the collection and focusing of long filament plasma-based THz pulses^[69].

4. Plasma lens array for axial magnetic field generation

The lenses we designed here are capable of not only achieving off-axis laser focusing but also demonstrating a greater range of application scenarios, such as the generation of ultra-strong magnetic fields, which is urgently required in laboratory astrophysics^[70] and high-energy-density physics^[52–54] for inertial confinement fusion^[52], particle acceleration^[53], magnetic reconnection^[54], etc. To the best of our knowledge, the development of such a magnetic field remains a significant challenge, primarily due to the inability of conventional LP laser beams to induce the requisite azimuthal current or equivalent angular momentum (AM)^[71]. In previous research, Shi *et al.*^[71] proposed a novel scheme for generating an axial magnetic field by employing

multiple laser beams with twisted pointing directions, which collectively interact with a plasma medium to induce the desired magnetic field. However, the generation of multiple laser beams in the experiment necessitates the utilization of multi-kJ PW-class laser systems, such as LFEX^[72] or NIF ARC^[73], thereby augmenting the complexity of the experimental setup.

Our proposed lens design exhibits off-axis focusing characteristics, enabling the implementation of multiple off-axis focusing lenses with distinct focal orientations to generate the aforementioned multi-beam laser pulses with twisted pointing directions. Thus, here we can use a beam-splitting array consisting of four plasma lenses previously designed to generate the strong axial magnetic field, as shown in Figure 7(a). The four off-axis lenses were set with distinct focal positions at $(21\lambda_0, 6\lambda_0, 0\lambda_0)$, $(21\lambda_0, 0\lambda_0, -6\lambda_0), (21\lambda_0, -6\lambda_0, 0\lambda_0)$ and $(21\lambda_0, 0\lambda_0, 6\lambda_0),$ respectively. Their density distribution within the array was systematically determined based on the refractive index profile, which can be referred to in Equation (2). The plasma target with a thickness of $5\lambda_0$, a density of $0.5n_c$ and a dimension of 20 μ m \times 20 μ m in the $y \times z$ directions was situated between $x = 12\lambda_0$ and $17\lambda_0$ behind the array. To generate a plasma lens array with distinct density distributions for each lens, we can employ a multi-nozzle 3D printer to deposit colloidal dispersions of varying concentrations in different regions. By adjusting the deposition paths and material ratios, the desired density gradients may be achieved^[63]. The incident laser electric field normalized amplitude is $a_0 = 1$. Upon passing through the first array, the incident Gaussian laser was split into four beams with twisted pointing directions, each of which can converge at a different point on the second plasma target. Here, the direction of each beam is indicated by the wave vector \mathbf{k}_i , with i denoting the serial number of the laser beam in question. The photon momentum in the ith beam is denoted by $p_i = \hbar k_i$. To understand the underlying physics, we consider two laser beams, $\mathbf{k}_{1,2} = (k_x, k_{\perp}^{1,2}, 0)$ intersecting the (y,z) plane at $z_{1,2} = \pm D_0$ and $y_{1,2} = 0$,

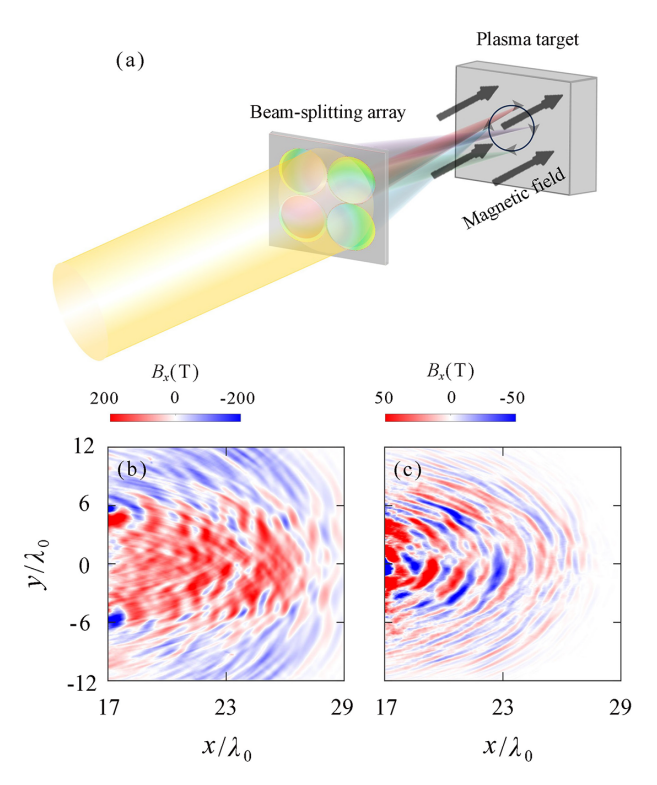


Figure 7. (a) Schematic diagram of an incident laser irradiating a beam-splitting array to divide into four beams with twisted pointing directions and illuminating four different locations on the plasma target. (b) Magnetic field distribution B_x (the incident laser passed through the array and interacted with the plasma target) in the (x, y) plane between $x = 17\lambda_0$ and $29\lambda_0$ at $t = 32T_0$. (c) The same as (b) without the array.

respectively, where D_0 is the beam offset. In this case, the axial AM of a given photon is given by $[r \times p]_{x}$, where r is the position vector and p is the photon momentum. As a result, the total AM of the two beams is given by $L_x \approx -N\hbar \left(k_{\perp}^1 - k_{\perp}^2\right) D_0/2^{[71]}$, where N is the number of photons in each laser beam. It can be inferred from this equation that if the two LP laser beams are tilted in the same direction, the AM remains 0. Conversely, if the two beams are tilted in opposite directions, the total AM is no longer 0. Thus, we can increase the AM by increasing the number of laser beams in a particular twist direction. Since the laser beam is distorted, the AM in this case is termed orbital angular momentum (OAM). During the interaction between the laser and the plasma, the OAM was transferred from the distorted lasers to the electrons eventually in the plasma, resulting in the generation of azimuthal currents, which can subsequently produce an axial magnetic field. This mechanism adheres to the principles of the Biot-Savart law^[74].

Figure 7(b) illustrates the distribution of the magnetic field B_x in the (x, y) plane at $t = 32T_0$. One sees that the magnetic field is distributed along the x-axis, with the field strength reaching up to 200 T. In order to facilitate comparative analysis, we remove the array while all other parameters remain unchanged. Figure 7(c) shows the distribution of B_x

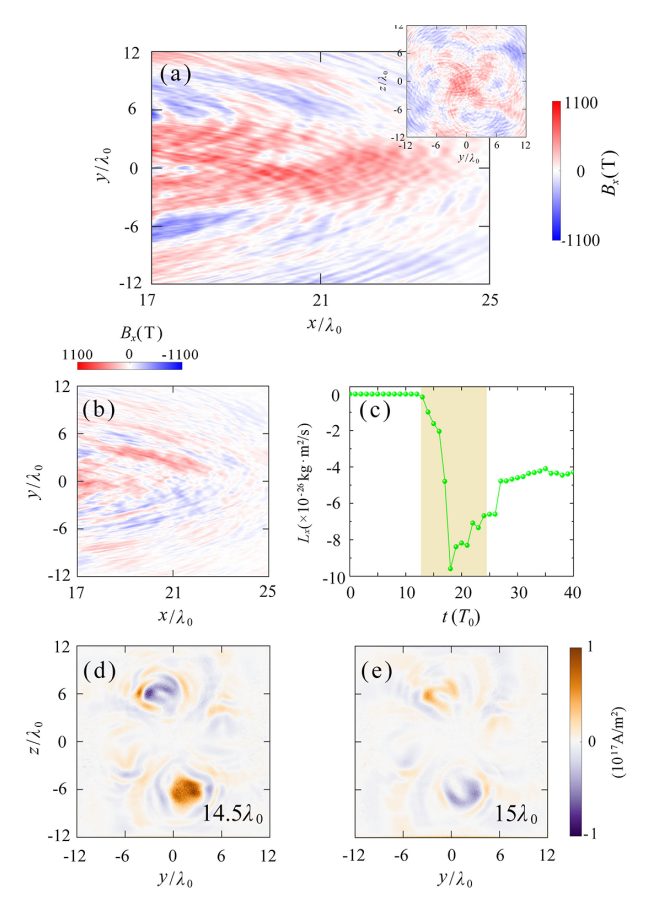


Figure 8. (a) Magnetic field distribution B_x (the incident laser passed through the array and interacted with the plasma target) in the (x, y) plane between $x = 17\lambda_0$ and $25\lambda_0$ at $t = 32T_0$. The inset in (a) shows the distribution of B_x on the (y, z) plane at $x = 23\lambda_0$. (b) Magnetic field distribution B_x (without the array) in the (x, y) plane between $x = 17\lambda_0$ and $25\lambda_0$ at $t = 32T_0$. (c) Evolution of the maximum value of the OAM of a single electron. The yellow shade here represents the stage when the laser is passing through the plasma target. (d) Azimuthal current density j_θ in the (y, z) plane of $x = 14.5\lambda_0$ and $(e) x = 15\lambda_0$ at $t = 18T_0$.

in the (x, y) plane for the reference simulation. Obviously, one did not observe an axial magnetic field in this simulation. This comparison highlights the feasibility of the proposed scheme for longitudinal magnetic field generation.

In order to verify the capability of the proposed scheme to achieve beam splitting at high laser intensities, we increase the incident laser parameter to $a_0 = 10$. The density of the plasma target is set to $3n_c$, the thickness is $5\lambda_0$ ($x = 12\lambda_0$ to $17\lambda_0$) and the dimensions of the simulated box remain unchanged. Figure 8(a) shows the resultant distribution of the magnetic field B_x in the (x,y) plane after the laser pulse passes through the plasma target. One sees that a much stronger axial magnetic field can be generated with the field strength up to 1160 T. For a reference simulation without the array, no axial magnetic field is generated, as illustrated in Figure 8(b). Figure 8(c) shows the evolution of the maximum value of the OAM of a single electron in the plasma target region over time. The yellow shade here represents the stage

when the laser is passing through the plasma target. It is evident that before the laser pulse interacts with the plasma target, the plasma electrons do not carry OAM. Conversely, when the laser pulses with the twisted pointing directions traverse the plasma target, a transfer of OAM from the laser pulses to the electrons occurs. This results in a substantial augmentation in the OAM of the electrons, reaching a maximum of approximately $9.3 \times 10^{-26} \text{ kg} \cdot \text{m}^2/\text{s}$ for a single electron at $t = 18T_0$. It is notable that the OAM exhibits a decline as the main pulse of the laser partially exits the plasma target region. However, the electrons in the plasma target region can still maintain the OAM after the laser has passed through the plasma target region. Figures 8(d) and 8(e) show the azimuthal current density j_{θ} at $x = 14.5\lambda_0$ and $x = 15\lambda_0$ in the plasma target region at $t = 18T_0$, respectively. One can see that when the laser pulses with a twisted pointing direction propagate in the plasma target, j_{θ} of about $1 \times 10^{17} \text{ A/m}^2$ can be generated at $x = 14.5\lambda_0$. Furthermore, a comparison between Figures 8(d) and 8(e) reveals a rotation in i_{θ} , which demonstrates that the OAM carried by the twisted laser pulse is effectively transferred to the electrons, inducing strong rotating currents. This finally leads to the generation of a strong axial magnetic field (>1000 T), and such a kiloteslalevel magnetic field may hold promise for applications in central-ignition inertial confinement fusion experiments^[51], sheath-based ion acceleration^[53], etc.

In order to explore the robustness of the proposed scenario, we performed simulations with the incident laser parameter ranging from $a_0 = 1$ to 10 and plasma target density from $n_{\rm e} = 0.5$ to 5. Figure 9(a) demonstrates that the generated axial magnetic field increases with the augmentation of the incident laser intensity. When $a_0 = 10$, a stronger axial magnetic field at the kilotesla level can be achieved. The blue dashed line in Figure 9(a) represents the critical density $\gamma_{\rm L} n_{\rm c}$ corresponding to different laser intensities. When the plasma target density exceeds the critical density, the incident laser pulse is unable to pass through the target, resulting in a substantial decrease in the axial magnetic field strength behind the target. Conversely, for the lower density plasma target, increasing the laser intensity can cause target disruption, thereby preventing axial magnetic field generation. Consequently, the generation of a strong axial magnetic field requires selecting a plasma target with a density marginally below the critical density while ensuring the preservation of target integrity. By fitting the simulation results, it is found that when n_e and a_0 satisfy the relationship $n_e \propto a_0^{3/2}$ (red solid line), the axial magnetic field strength is maximum. Furthermore, we investigated the evolution of maximum magnetic field strength for different laser parameters and plasma target densities, as shown in Figure 9(b). Here, we calculate the maximum axial magnetic field strengths generated by incident laser parameters ranging from $a_0 = 1$ to 10 and fit the obtained results to explore the underlying physics. It is interesting to see that the maximum axial

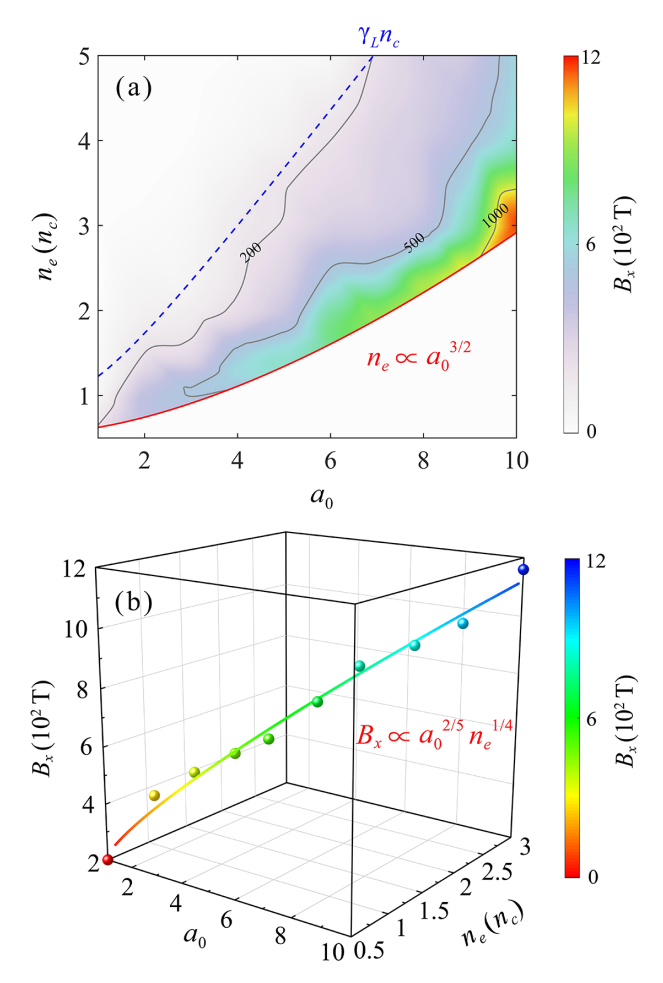


Figure 9. (a) Trend of the axial magnetic field B_x along with the incident laser parameter a_0 and plasma target density n_e . The fitting line (red solid line) refers to the maximum magnetic field strength at different laser parameters and plasma target densities. The blue dashed line marks the critical density of the plasma. (b) Evolution of maximum magnetic field strength for different laser parameters and plasma target densities.

magnetic field strength increases progressively with augmentation of the incident laser intensity, reaching approximately kilotesla-level magnitudes at $a_0 = 9$. In particular, it reveals a relationship $B_x \propto a_0^{2/5} \cdot n_{\rm e}^{1/4}$ from 3D-PIC simulations. Considering the relationship $n_{\rm e} \propto a_0^{3/2}$, we can get approximately $B_x \propto a_0^{3/4}$ and $B_x \propto n_{\rm e}^{1/2}$, respectively. Taking the incident laser parameter $a_0 = 50$ for example, a stronger axial magnetic field at $B_x \geq 3500$ T can be achieved. This demonstrates the robustness of our scenario in generating a strong axial magnetic field at kilotesla-level magnitudes.

5. Conclusion

In summary, we propose a novel plasma-based focusing lens with a density gradient to produce a relativistic focused laser pulse in a tunable focal volume. 3D-PIC simulations have demonstrated that the focal radius of the output laser can

reach approximately 2.3 µm, reduced by a factor of four in comparison to the incident Gaussian laser, with the focused laser intensity reaching up to 10¹⁹ W/cm² and the energy transmission efficiency as high as 61.16%. Furthermore, by modifying the orientation of the plasma density gradient, the laser focus can be meticulously regulated and positioned at the particularly desired location, thereby facilitating off-axis focusing. In consideration of the aforementioned controllable focal point, a distinctive beam-splitting array has been designed to split an incident Gaussian laser into multiple laser beams with twisted pointing directions, making it possible to generate a strong axial magnetic field (>1000 T). Our scheme may open up a new avenue for plasma optics and nonlinear optics, and would find various potential applications in intense laser-plasma interaction from high-energydensity physics to laboratory astrophysics, etc.

Acknowledgements

This work was supported by the National Natural Science Foundation of China (Grant Nos. 12375244 and 12135009) and the Natural Science Foundation of Hunan Province of China (Grant No. 2025JJ30002).

References

- 1. D. Strickland and G. Mourou, Opt. Commun. **55**, 447 (1985).
- I. N. Ross, P. Matousek, M. Towrie, A. J. Langley, and J. L. Collier, Opt. Commun. 144, 125 (1997).
- X. L. Zhu, T. P. Yu, Z. M. Sheng, Y. Yin, I. C. E. Turcu, and A. Pukhov, Nat. Commun. 7, 13686 (2016).
- M. J. Duff, R. Capdessus, C. P. Ridgers, and P. McKenna, Plasma Phys. Control. Fusion 61, 094001 (2019).
- T. P. Yu, K. Liu, J. Zhao, X. L. Zhu, Y. Lu, Y. Cao, H. Zhang, F. Q. Shao, and Z. M. Sheng, Rev. Mod. Plasma Phys. 8, 24 (2024)
- M. Lobet, X. Davoine, E. d'Humières, and L. Gremillet, Phys. Rev. Accel. Beams 20, 043401 (2017).
- 7. A. Di Piazza, C. Müller, K. Z. Hatsagortsyan, and C. H. Keitel, Rev. Mod. Phys. **84**, 1177 (2012).
- 8. J. H. Cheng, Y. Li, and T. P. Yu, Phys. Rev. C **105**, 024312 (2022).
- Y. Y. Xu, J. H. Cheng, Y. T. Zou, Q. Xiao, and T. P. Yu, Phys. Rev. C 110, 064621 (2024).
- 10. A. B. Zylstra, O. A. Hurricane, D. A. Callahan, A. L. Kritcher, J. E. Ralph, H. F. Robey, J. S. Ross, C. V. Young, K. L. Baker, D. T. Casey, T. Döppner, L. Divol, M. Hohenberger, S. Le Pape, A. Pak, P. K. Patel, R. Tommasini, S. J. Ali, P. A. Amendt, L. J. Atherton, B. Bachmann, D. Bailey, L. R. Benedetti, L. Berzak Hopkins, R. Betti, S. D. Bhandarkar, J. Biener, R. M. Bionta, N. W. Birge, E. J. Bond, D. K. Bradley, T. Braun, T. M. Briggs, M. W. Bruhn, P. M. Celliers, B. Chang, T. Chapman, H. Chen, C. Choate, A. R. Christopherson, D. S. Clark, J. W. Crippen, E. L. Dewald, T. R. Dittrich, M. J. Edwards, W. A. Farmer, J. E. Field, D. Fittinghoff, J. Frenje, J. Gaffney, M. Gatu Johnson, S. H. Glenzer, G. P. Grim, S. Haan, K. D. Hahn, G. N. Hall, B. A. Hammel, J. Harte, E. Hartouni, J. E. Heebner, V. J. Hernandez, H. Herrmann, M. C. Herrmann, D. E. Hinkel, D. D. Ho, J. P. Holder, W. W. Hsing, H. Huang, K. D. Humbird, N. Izumi, L. C. Jarrott, J. Jeet, O. Jones, G. D. Kerbel, S. M. Kerr, S. F. Khan, J. Kilkenny,

- Y. Kim, H. Geppert Kleinrath, V. Geppert Kleinrath, C. Kong, J. M. Koning, J. J. Kroll, M. K. G. Kruse, B. Kustowski, O. L. Landen, S. Langer, D. Larson, N. C. Lemos, J. D. Lindl, T. Ma, M. J. MacDonald, B. J. MacGowan, A. J. Mackinnon, S. A. MacLaren, A. G. MacPhee, M. M. Marinak, D. A. Mariscal, E. V. Marley, and L. Masse, Nature 603, E34 (2022).
- X. Xu, Y. Zhang, H. Zhang, H. Lu, W. Zhou, C. Zhou, B. Dromey, S. Zhu, M. Zepf, X. He, and B. Qiao, Optica 7, 355 (2020).
- B. Shao, Y. Li, Y. Peng, P. Wang, J. Qian, Y. Leng, and R. Li, Opt. Lett. 45, 2215 (2020).
- C. Thaury, F. Quéré, J. P. Geindre, A. Levy, T. Ceccotti, P. Monot, M. Bougeard, F. Réau, P. D Oliveira, P. Audebert, R. Marjoribanks, and P. Martin, Nat. Phys. 3, 424 (2007).
- A. Leblanc, A. Denoeud, L. Chopineau, G. Mennerat, P. Martin, and F. Quéré, Nat. Phys. 13, 440 (2017).
- D. Turnbull, P. Michel, T. Chapman, E. Tubman, B. B. Pollock,
 C. Y. Chen, C. Goyon, J. S. Ross, L. Divol, N. Woolsey, and J.
 D. Moody, Phys. Rev. Lett. 116, 205001 (2016).
- M. S. Hur, B. Ersfeld, H. Lee, H. Kim, K. Roh, Y. Lee, H. S. Song, M. Kumar, S. Yoffe, D. A. Jaroszynski, and H. Suk, Nat. Photonics 17, 1074 (2023).
- 17. J. Ren, W. Cheng, S. Li, and S. Suckewer, Nat. Phys. 3, 732 (2007).
- T. M. Jeong, S. V. Bulanov, P. Valenta, G. Korn, T. Z. Esirkepov, J. K. Koga, A. S. Pirozhkov, M. Kando, and S. S. Bulanov, Phys. Rev. A 104, 053533 (2021).
- N. Li, D. Zou, N. Zhao, X. Jiang, F. Shao, and T. Yu, Opt. Express 30, 39631 (2022).
- M. R. Edwards and P. Michel, Phys. Rev. Appl. 18, 024026 (2022).
- H. Y. Wang, C. Lin, Z. M. Sheng, B. Liu, S. Zhao, Z. Y. Guo, Y. R. Lu, X. T. He, J. E. Chen, and X. Q. Yan, Phys. Rev. Lett. 107, 265002 (2011).
- C. Ren, B. J. Duda, R. G. Hemker, W. B. Mori, T. Katsouleas, T. M. Antonsen, and P. Mora, Phys. Rev. E 63, 026411 (2001).
- 23. J. B. Rosenzweig and P. Chen, Phys. Rev. D 39, 2039 (1989).
- 24. M. Jirka, O. Klimo, and M. Matys, Phys. Rev. Res. **3**, 033175 (2021).
- L. Wang, W. Liu, Q. Jia, and J. Zheng, Plasma Phys. Control. Fusion 65, 055006 (2023).
- H. Zhang, Q. Li, C. Zheng, J. Zhao, Y. Lu, D. Li, X. Xu, K. Liu, Y. Tian, Y. Lin, F. Zhang, and T. Yu, Opt. Express 30, 29388 (2022).
- T. S. Hung, C. H. Yang, J. Wang, S. Y. Chen, J. Y. Lin, and H. H. Chu, Appl. Phys. B 117, 1189 (2014).
- H. Chen, W. Yu, X. Xu, J. Jiao, Y. Wei, X. Jiang, Y. Yin, T. Yu, H. Zhuo, and D. Zou, High Power Laser Sci. Eng. 13, e1 (2025).
- X. Wang, M. Krishnan, N. Saleh, H. Wang, and D. Umstadter, Phys. Rev. Lett. 84, 5324 (2000).
- 30. M. Liu, W. M. Wang, and Y. T. Li, Phys. Rev. E **109**, 015208 (2024).
- T. Ziegler, I. Göthel, S. Assenbaum, C. Bernert, F.-E. Brack, T. E. Cowan, N. P. Dover, L. Gaus, T. Kluge, S. Kraft, F. Kroll, J. Metzkes-Ng, M. Nishiuchi, I. Prencipe, T. Püschel, M. Rehwald, M. Reimold, H.-P. Schlenvoigt, M. E. P. Umlandt, M. Vescovi, U. Schramm, and K. Zeil, Nat. Phys. 20, 1211 (2024).
- 32. L. Reichwein, A. Pukhov, and M. Büscher, Phys. Rev. Accel. Beams **25**, 081001 (2022).
- 33. U. Teubner and P. Gibbon, Rev. Mod. Phys. 81, 445 (2009).
- 34. R. A. Ganeev, Appl. Phys. B 129, 17 (2023).
- M. Venkatesh, R. A. Ganeev, V. V. Kim, G. S. Boltaev, I. B. Sapaev, J. Liang, J. Yu, and W. Li, Opt. Express 30, 17080 (2022).

S. Corde, K. Ta Phuoc, G. Lambert, R. Fitour, V. Malka, A. Rousse, A. Beck, and E. Lefebvre, Rev. Mod. Phys. 85, 1 (2013).

10

- K. Xue, Z. K. Dou, F. Wan, T. P. Yu, W. M. Wang, J. R. Ren,
 Q. Zhao, Y. T. Zhao, Z. F. Xu, and J. X. Li, Matter Radiat.
 Extrem. 5, 054402 (2020).
- E. D. Filippov, S. S. Makarov, K. F. Burdonov, W. Yao, G. Revet, J. Béard, S. Bolaños, S. N. Chen, A. Guediche, J. Hare, D. Romanovsky, I. Y. Skobelev, M. Starodubtsev, A. Ciardi, S. A. Pikuz, and J. Fuchs, Sci. Rep. 11, 8180 (2021).
- 39. R. Betti and O. A. Hurricane, Nat. Phys. 12, 435 (2016).
- 40. Y. Guo, X. Zhang, D. Xu, X. Guo, B. Shen, and K. Lan, Matter Radiat. Extrem. **8**, 035902 (2023).
- M. R. Edwards, V. R. Munirov, A. Singh, N. M. Fasano, E. Kur, N. Lemos, J. M. Mikhailova, J. S. Wurtele, and P. Michel, Phys. Rev. Lett. 128, 065003 (2022).
- 42. M. Khorasaninejad, W. T. Chen, J. Oh, and F. Capasso, Nano Lett. 16, 3732 (2016).
- 43. Y. Zhou, R. Chen, and Y. Ma, Opt. Lett. 42, 4716 (2017).
- A. Y. Zhu, W. T. Chen, J. Sisler, K. M. A. Yousef, E. Lee, Y. W. Huang, C. W. Qiu, and F. Capasso, Adv. Opt. Mater. 7, 1801144 (2019).
- A. Y. Zhu, W. T. Chen, M. Khorasaninejad, J. Oh, A. Zaidi,
 I. Mishra, R. C. Devlin, and F. Capasso, APL Photonics 2, 036103 (2017).
- M. Khorasaninejad, W. T. Chen, J. Oh, and F. Capasso, Nano Lett. 16, 3732 (2016).
- 47. Y. Zhou, R. Chen, and Y. Ma, Opt. Lett. 42, 4716 (2017).
- 48. S. H. Seo, J. M. Ryu, and H. Choi, Appl. Sci. 10, 7931 (2020).
- A. J. Gonsalves, K. Nakamura, C. Lin, D. Panasenko, S. Shiraishi, T. Sokollik, C. Benedetti, C. B. Schroeder, C. G. R. Geddes, J. van Tilborg, J. Osterhoff, E. Esarey, C. Toth, and W. P. Leemans, Nat. Phys. 7, 862 (2011).
- J. D. Mullett, R. Dodd, C. J. Williams, G. Triantos, G. Dearden, A. T. Shenton, K. G. Watkins, S. D. Carroll, A. D. Scarisbrick, and S. Keen, J. Phys. D: Appl. Phys. 40, 4730 (2007).
- P. Y. Chang, G. Fiksel, M. Hohenberger, J. P. Knauer, R. Betti,
 F. J. Marshall, D. D. Meyerhofer, F. H. Séguin, and R. D. Petrasso, Phys. Rev. Lett. 107, 035006 (2011).
- 52. E. Lindman, High Energy Density Phys. 6, 227 (2010).
- K. Weichman, A. P. L. Robinson, M. Murakami, J. J. Santos, S. Fujioka, T. Toncian, J. P. Palastro, and A. V. Arefiev, Phys. Plasmas 29, 053104 (2022).
- H. Huang, Y. Hu, Y. Ping, and T. Yu, Geophys. Res. Lett. 50, e2023GL104868 (2023).
- 55. G. Sun, E. Ott, Y. C. Lee, and P. Guzdar, Phys. Fluids **30**, 526 (1987)

- 56. C. B. Boyer, Science 181, 152 (1973).
- T. D. Arber, K. Bennett, C. S. Brady, A. Lawrence-Douglas, M. G. Ramsay, N. J. Sircombe, P. Gillies, R. G. Evans, H. Schmitz, A. R. Bell, and C. P. Ridgers, Plasma Phys. Control. Fusion 57, 113001 (2015).
- T. Long, C. Zhou, L. Ju, T. Huang, M. Yu, K. Jiang, C. Wu, S. Wu, H. Zhang, B. Qiao, S. Ruan, and X. He, Phys. Rev. Res. 2, 033145 (2020).
- L. Zhou, Z. Yang, J. Yang, Y. Wu, and D. Wei, Chem. Phys. Lett. 677, 7 (2017).
- T. Long, C. Zhou, S. Wu, L. Ju, K. Jiang, R. Bai, T. Huang, H. Zhang, M. Yu, S. Ruan, and X. He, Phys. Rev. E 103, 023204 (2021)
- Y. Jiang, Z. Xu, T. Huang, Y. Liu, F. Guo, J. Xi, W. Gao, and C. Gao, Adv. Funct. Mater. 28, 1707024 (2018).
- 62. H. Sun, Z. Xu, and C. Gao, Adv. Mater. 25, 2554 (2013).
- Q. Cheng, Z. Sheng, Y. Ding, Y. Li, and X. Zhang, Prog. Mater. Sci. 152, 101456 (2025).
- 64. E. Hecht, Optik (Walter de Gruyter GmbH & Co KG, 2023).
- A. Y. Zhu, W. T. Chen, M. Khorasaninejad, J. Oh, A. Zaidi, I. Mishra, R. C. Devlin, and F. Capasso, APL Photonics 3, 036103 (2017).
- T. Tajima and V. Malka, Plasma Phys. Control. Fusion 62, 034004 (2020).
- A. Pazzaglia, L. Fedeli, A. Formenti, A. Maffini, and M. Passoni, Commun. Phys. 3, 133 (2020).
- N. Saedjalil, M. Mehrangiz, S. Jafari, and A. Ghasemizad, Eur. Phys. J. Plus 131, 188 (2016).
- R. T. Paulino, B. Colmey, and D. G. Cooke, Opt. Express 32, 26351 (2024).
- 70. P. Korneev, E. d'Humières, and V. Tikhonchuk, Phys. Plasmas **21**, 022117 (2014).
- Y. Shi, A. Arefiev, J. X. Hao, and J. Zheng, Phys. Rev. Lett. 130, 155101 (2023).
- J. Kawanaka, N. Miyanaga, H. Azechi, T. Kanabe, T. Jitsuno, K. Kondo, Y. Fujimoto, N. Morio, S. Matsuo, Y. Kawakami, R. Mizoguchi, K. Tauchi, M. Yano, S. Kudo, and Y. Ogura, J. Phys.: Conf. Ser. 112, 032006 (2008).
- 73. J. K. Crane, G. Tietbohl, P. Arnold, E. S. Bliss, C. Boley, G. Britten, G. Brunton, W. Clark, J. W. Dawson, S. Fochs, R. Hackel, C. Haefner, J. Halpin, J. Heebner, M. Henesian, M. Hermann, J. Hernandez, V. Kanz, B. McHale, J. B. McLeod, H. Nguyen, H. Phan, M. Rushford, B. Shaw, M. Shverdin, R. Sigurdsson, R. Speck, C. Stolz, D. Trummer, J. Wolfe, J. N. Wong, G. C. Siders, and C. P. J. Barty, J. Phys.: Conf. Ser. 244, 032003 (2010).
- 74. J. D. Jackson, *Electrodynamics* (John Wiley & Sons, 2007).